Title

Role of Polyacrylic Acid (PAA) Binder on the Solid Electrolyte Interphase in Silicon Anodes

Authors

Parikh, Pritesh
Sina, Mahsa
Banerjee, Abhik
et al.

Peer reviewed

Role of Polyacrylic Acid (PAA) Binder on the Solid Electrolyte Interphase in Silicon Anodes

Pritesh Parikh,[†] Mahsa Sina,[†] Abhik Banerjee,[†] Xuefeng Wang,[†] Macwin Savio D'Souza,[†] Jean-Marie Doux,[†] Erik A. Wu,[†] Osman Y. Trieu,[†] Yongbai Gong,[†] Qian Zhou,[‡] Kent Snyder,[‡] and Ying Shirley Meng*,[†]

[†]Department of NanoEngineering, University of California San Diego, 9500 Gilman Drive, La Jolla, California 92093, United States
[‡]Energy Storage Research Department, Ford Motor Company, 2101 Village Road, Dearborn, Michigan 48124, United States

Ⓢ *Supporting Information*

ABSTRACT: To obtain high-energy density Li-ion batteries for the next-generation storage devices, silicon anodes provide a viable option because of their high theoretical capacity, low operating potential versus lithium (Li), and environmental abundance. However, the silicon electrode suffers from large volume expansion (∼300%) that leads to mechanical failure, cracks in the SEI (solid electrolyte interphase), and loss of contact with the current collector, all of which severely impede the capacity retention. In this respect, the choice of binders, carbon, electrolyte, and the morphology of the silicon itself plays a critical role in improving capacity retention. Of specific mention is the role of binders where a carboxylic acid-heavy group, PAA (polyacrylic acid), has been demonstrated to have better cycling capacity retention as compared to CMC (carboxy methyl cellulose). Traditionally, the role of binders has been proposed as a soft matrix backbone that allows volume expansion of the anode while preserving its morphology. However, the effect of the binder on both the rate of formation of SEI species across cycles and its distribution around the silicon nanoparticles has not been completely investigated. Herein, we use two different binders (PAA and CMC) coupled with LiFSI (lithium bis(fluorosulfonyl)imide)/EMI-FSI (1-ethyl-3-methylimidazolium bis(fluorosulfonyl)imide) ionic liquid as the electrolyte to understand the effect of binder on the SEI. Using STEM-EDX (scanning transmission electron microscopy–energy-dispersive X-ray spectroscopy), EELS (electron energy loss spectroscopy), and XPS (X-ray photoelectron spectroscopy), we discuss the evolution of the SEI on the Si electrode for both binders. Our results indicate that a faster decomposition of FSI^- with a PAA binder leads to LiF (lithium fluoride) formation, making F^- unavailable for subsequent SEI formation cycles. This allows further decomposition of the LiFSI salt to sulfates and sulfides which form a crucial component of the SEI around silicon nanoparticles after 100 cycles in the PAA binder-based system. The dual effects of faster consumption of F^- to form LiF together with the distribution of passivating sulfides in the SEI could allow for better capacity retention in the PAA binder system as compared to that with CMC.
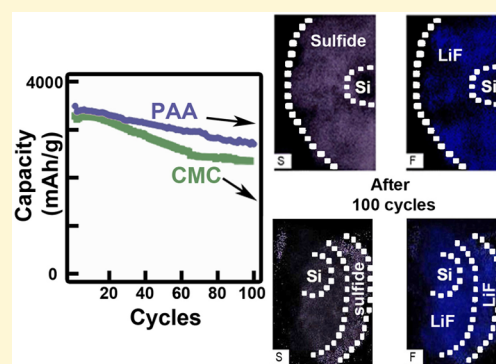
1. INTRODUCTION

The ability to engineer a sustainable and green future presents a formidable challenge to governments and industries alike. Regular reports of Antarctic ice melts,[1] increase in respiratory issues in both developing and developed countries,[2] and the alarming increase in the rate of global greenhouse gas emissions[3,4] all point to the gravity of the situation at hand. Photovoltaics, wind, tidal, and geothermal energy all provide renewable sources with minimal carbon footprints but the intermittency in the generation warrants the need for energy storage solutions. Li-ion batteries have evolved to form a pivotal role in this ever-changing energy landscape. With its foray into the electric car and the grid storage markets, in the span of a decade, Li-ion batteries have taken the center stage in energy storage.

Since its introduction by Sony in 1991, the cathode consisting of LCO (lithium cobalt oxide) has seen improvements with different chemistries based on Ni, Co, and Mn to enable high-voltage operation (>4.3 V), higher specific capacity (>200 mA h/g), and greater capacity retention.[5] Currently, NCM (lithium nickel manganese cobalt oxide) and NCA (lithium nickel cobalt aluminum oxide) are the two cathode options with continuous research and development toward novel chemistries and optimal Ni/Co and Co/Mn ratios. On the anode side, graphite continues to be the material of choice, providing 372 mA h/g theoretical specific capacity. However, to develop the next generation of batteries, the specific capacity should be increased

to 1000 mA h/g.[6] To this effect, research on anodes has explored hard carbons, oxides, sulfides, phosphides, nitrides, alloy anodes, and more recently even graphene/rGO (reduced graphite oxide) and CNTs (carbon nanotubes).[5,7]

Although hard carbon, due to the presence of nanograins and voids, allows a theoretical capacity larger than graphite, it also leads to greater solid electrolyte interphase (SEI) formation, limiting the first cycle Coulombic efficiency. Oxides such as LTO (lithium titanium oxide) provide high thermal stability and high safety but suffer from low-energy density. Sulfides, phosphides, and nitrides all provide high specific capacity and low operation potential versus Li but suffer from poor capacity retention and high cost of production.[8]

In this respect, alloy anodes provide high specific and volumetric energy densities amongst all anode chemistries. Among alloy anodes, Si, Ge, Al, Sn, and Sb are all potential candidates to replace graphite, but they all suffer from severe volume expansion that is currently limiting their commercial adoption. Si, due to its abundance (leading to potentially low production costs), environmentally benign nature at the macroscale, high specific capacity (~4200 mA h/g theoretical), and low operating voltage versus Li (compared to other alloy anodes), forms a natural choice of anode material.[7,9] However, the volume expansion and subsequent contraction present a host of different issues: (a) the SEI layer undergoes continuous fracture during cycling, exposing fresh silicon surface to the electrolyte and formation of new SEI. Thus, silicon sees a gradual increase in the SEI layer thickness and electrolyte consumption which is detrimental to capacity retention. (b) The volume expansion also creates large stresses on the silicon particle itself that leads to pulverization. This can result in a loss of usable active material, trapping of Li^+ in the anode host due to reduced diffusion across different particles, a thicker SEI layer, and increased possibility of reaction with surface oxides. (c) The pulverization and volume expansion/contraction further contribute to delamination and/or loss of electrical contact with the current collector leading to a rapid capacity drop after a few cycles.[9]

To address these issues, a variety of different solutions have been provided and explored (some of which are mentioned here) such as the use of active and inactive alloys, intermetallics, porous silicon, core−shell structures, and uniform carbon coatings. Tamirat et al. demonstrated that through the use of intermetallics (Mg_2Si) one can limit the capacity obtained (compared to the theoretical capacity) and hence the associated volume expansion.[10] Wang et al. prepared a novel monodisperse silicon electrode through Mg-isothermic reaction followed by chemical vapor deposition with acetylene to give a uniform carbon composite coating, thus providing a cushioning effect to accommodate the stresses involved with volume expansion.[11] Restricting the operating voltage is another way to limit the depth of discharge and hence the volume expansion, which was carried out by Wu et al. on silicon thin-film electrodes.[12] On the other hand, both thin films and different nanoparticle morphologies as well as porous Si particles can be used to accommodate the stress and prevent any pulverization.[12−17] Liu et al. demonstrated that Si particles with a size below 150 nm can suppress the stress associated with volume expansion in silicon without any cracks or fracture.[18] Amongst all of these strategies, intermetallics and composites reduce the active material available to host the Li, reducing the energy density, whereas the disadvantage for nanoparticles and thin films is their higher cost of fabrication.

Hence, the ability to form a matrix that can effectively buffer the volume expansion associated with silicon and still be commercially adaptable has still not been completely explored. For the silicon electrode, the binder can thus play this very critical role of forming a soft matrix that can provide both the required mechanical and electrochemical stability/electronic conductivity. In this respect, engineering a binder which forms a small portion of the total cost and fabrication process provides a very reliable strategy to improve the Si anode performance. The exploration of different branched and co-polymers as binders for silicon anodes is now an active and burgeoning field of research. Choi et al. demonstrated stable capacity over 3000 mA h/g with micro-silicon particles and a novel polyrotaxane-based binder.[19] Liu et al. also prepared a polyfluorene (PF) based conductive binder to overcome the volume expansion and resulting electrical isolation.[20] Wang et al. prepared a self-healing polymer based on dynamic hydrogen-bonding sites to allow the micro-silicon particles to obtain a stable capacity over 2000 mA h/g after 130 cycles.[21] Wu et al. have also proposed the components required for the design of an optimized ideal binder with PF groups for electronic conductivity and methyl benzoate esters for mechanical strength.[22] Amongst the traditional binders though, polyacrylic acid (PAA)-derived polymers have shown enhanced capacity retention over 100 cycles as compared to that for carboxy methyl cellulose (CMC), alginate, and PVDF (polyvinylidene fluoride) binders because of their superior mechanical strength.[23−25] The PAA binder contains a larger number of −COOH (carboxylic acid) groups that are proposed to have a positive effect on the silicon electrode through hydrogen bonding with the SiO_x terminated surface, thus allowing the pulverized Si particles to still maintain contact with the current collector. While the role of the binder from a mechanical aspect and its effect on electrochemical performance are largely well explored through peel strength tests, adhesion tests, and stress−strain studies,[19,26,27] its interaction with the electrolyte and ultimately on the formation of the SEI has not been well understood to date. For the silicon electrodes, the SEI chemical composition and its spatial distribution are important aspects because a stable SEI can lead to lower electrolyte consumption for a system with such a large volume expansion. In this respect, the role of the binder and how it affects the rate of decomposition of the electrolyte to form SEI species, its ability to affect the formation of different SEI species across cycles, and the spatial distribution of the SEI are all important aspects that warrant further study. Understanding this process would lead to the design of better binders that interact favorably to form a more stable SEI.

Hence, in this study, we use Si nanoparticles with two different binders (PAA and CMC) and ionic liquid (IL) electrolyte as a model system to understand the mechanism of how the binder affects the chemical composition and nanoscale distribution of the SEI components. Using EDX (energy-dispersive X-ray spectroscopy) and EELS (electron energy-loss spectroscopy) in the TEM (transmission electron microscope) and XPS (X-ray photoelectron spectroscopy), we can observe the evolution of the SEI for electrodes with PAA and CMC binders. The interaction between the binder and electrolyte on the Si anode occurs differently with each binder. The results and proposed mechanism are discussed here.

The IL with LiFSI (electrolyte salt) is chosen as the electrolyte of choice because it has been shown to have better electrochemical performance compared to traditional carbonate-based electrolytes.[17,28] It is also reported that LiFSI salt decomposes
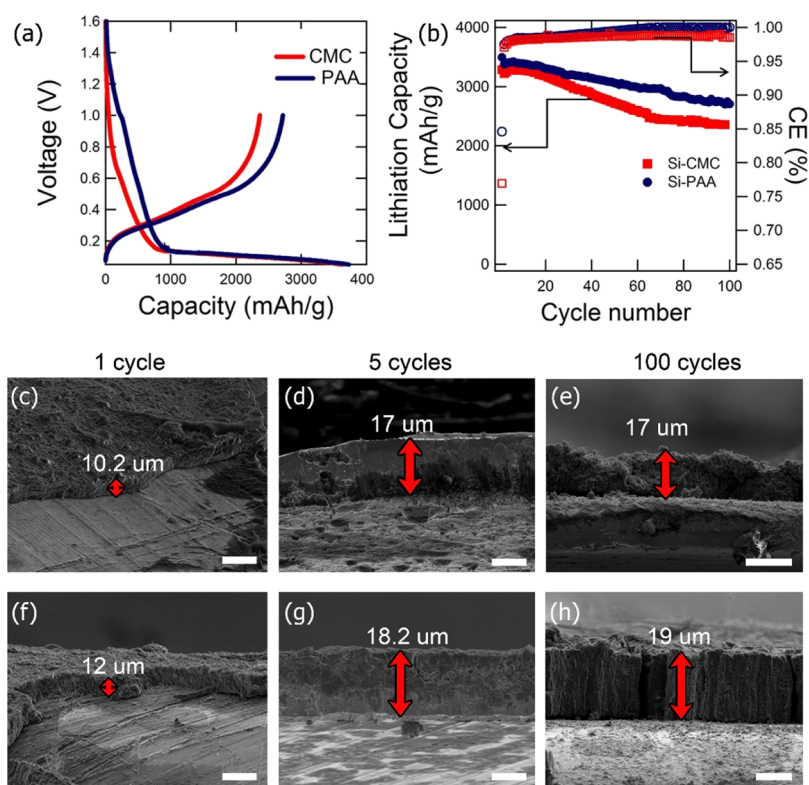
Figure 1. [a] First cycle voltage profile for electrodes with CMC and PAA binders. Electrodes with PAA binder show larger delithiation capacity compared to electrodes with CMC binder. [b] Lithiation capacity and Coulombic efficiency plotted as a function of cycle number. Greater capacity retention is seen in the PAA samples as compared to that for CMC after 100 cycles, even though they both start off similarly. [c] Expansion in the Si anodes seen as a function of cycling using cross-sectional SEM. Both CMC (c–e) and PAA (f–h) show similar volume expansion of 200% after 100 cycles. The CMC electrodes also show propagation of cracks that can affect the electrode capacity retention. PAA binder allows the electrode morphology to be preserved even after 100 cycles. The scale bar is 20 μm for each image.

on the silicon electrode surface to form a stable LiF film that impedes further electrolyte decomposition.[29] The definitive action of LiF has been well documented when FEC is used as an additive in carbonate-based electrolytes.[30−32]

2. METHODS

2.1. Electrode Fabrication. Si nanoparticles (average particle size: 50 nm, Alfa Aesar) were used as the active material of the electrode. The Si composite anode was fabricated as follows: 50 wt % nano-Si powder, 25 wt % Ketjenblack (EC-600JD, AkzoNobel), and 25 wt % binder. A Si/C composite was first prepared by mixing 0.504 g of Si and 0.252 g of Ketjenblack in a glovebox and milled (outside the glovebox) at 300 rpm for 46 min with a 15 min rest period. The binder solution (dissolved in deionized water) was added next to the Si/C composite. For the binder in one case, a CMC-Na (sodium CMC, M_w 250,000, Sigma-Aldrich) solution in deionized water was used. A 3.2 wt % solution of CMC was prepared. The PAA binder was prepared in a similar fashion using a 6.25 wt % PAA solution in deionized water (PAA M_v of 450,000 Da and obtained from Sigma-Aldrich).

The obtained slurry was coated on a copper foil by using a doctor blade, and the as-prepared electrode was dried at 80 °C overnight under a vacuum to completely remove residual water in the electrode. The electrode sheet was cut into a disk and used for the battery tests. The mass of the Si active material on the electrode was ~0.45−0.5 mg/cm², which is equivalent to 1.6 mA h/cm². This electrode was assembled in a 2032 coin cell using a polymer separator (C480, Celgard Inc., USA). The IL electrolyte was prepared by dissolving lithium bis-(fluorosulfonyl)imide, LiFSI (Nippon Shokubai Co., Ltd.) in 1-ethyl-3-methylimidazolium bis(fluorosulfonyl)imide, EMIFSI (Solvionic Co., Ltd.) at a concentration of 0.6 mol/kg and was used without further purification. This electrolyte is referred to as LiFSI/EMIFSI. The battery-grade lithium metal was chosen as the counter electrode.

Coin cells were assembled in a glovebox purged with high purity Ar gas and maintained at a moisture level at or below 5 ppm.

2.2. Electrochemical Tests. The coin cells were assembled, and electrochemical performance tests were performed using an Arbin battery cycler in the galvanostatic mode, limiting the charge and discharge potentials to 1.0 and 0.05 V versus the Li counter electrode, respectively (note that "discharge" here refers to lithium alloying into the Si anode or lithiation). The open-circuit voltage of the coin cells was monitored for 10 h, and then the cells were charged and discharged at a C-rate of C/20 for the formation cycle and C/10 for subsequent cycles. The percent capacity retention was calculated with respect to the first discharge capacity. All electrochemical measurements were carried out at 20 °C.

2.3. Scanning Electron Microscopy. After electrochemical cycling, the coin cells were disassembled and the Si anodes were rinsed with acetonitrile to remove the residual electrolyte and dried in an Ar-filled glovebox. The surface and cross-sectional images of the Si anode were collected with a field emission environmental scanning electron microscopy (SEM).

2.4. X-ray Photoelectron Spectroscopy. The chemical compositions of Si anode surfaces were analyzed after 1 and 100 electrochemical cycles, using XPS. All cycled samples were measured at the end of the cycle (each cycle consists of charge and discharge). The coin cells were disassembled in an Ar-filled glovebox, Si anodes were rinsed with acetonitrile and transferred in a vacuum tube to the glovebox connected to the XPS chamber, and samples were not exposed to air. The washed electrodes were transferred to the ultrahigh-vacuum environment using an in-house sealed container used for transferring air-sensitive samples. XPS was performed using a Kratos Axis Supra XPS. All XPS measurements were collected with a 300 μm × 700 μm spot size without using a charge neutralizer during acquisition. Survey scans were collected with a 1.0 eV step size and were followed by high-
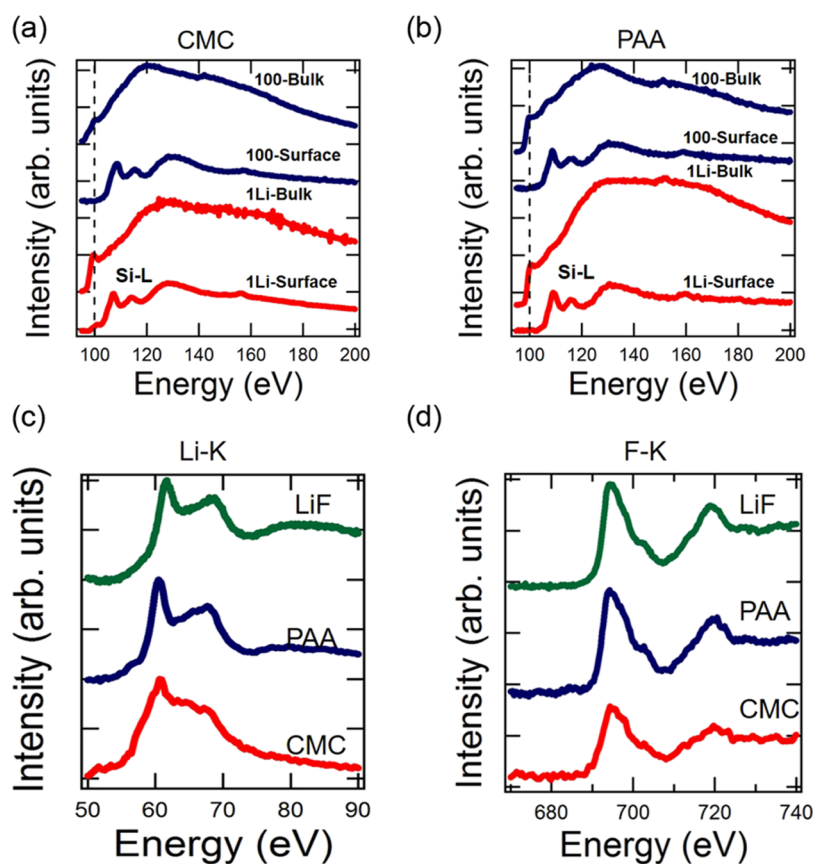
Figure 2. EELS spectra of Si-L edge (a,b), indicating the electrode surface and bulk comparison. The Si-L edge indicates the presence of a native oxide layer on the surface with both the binders. Li-K edge (c) and F-K edge (d) for both CMC and PAA binders indicate the formation of LiF after the 1st cycle.

resolution scans with a step size of 0.1 eV for carbon 1s, sulfur 2p, and fluorine 1s regions.

2.5. Electron Energy-Loss Spectroscopy. The electrochemical cells were disassembled in an argon-filled glovebox, and the electrodes were washed with acetonitrile. The washed electrodes were then scraped to collect powdered electrode flakes. A small amount of powder was placed on a TEM Lacey carbon film supported on a copper grid. SAED (selected area diffraction patterns), ADF-STEM (annular dark-field scanning transmission electron microscopy) images, and EELS were acquired using a JEOL 2010F operated at 197 kV and equipped with a Gatan GIF 200 spectrometer. The EELS spectra were obtained with a collection half angle of 27 mrad and a convergence angle of 10 mrad and with an energy resolution of 0.9 eV. Additionally, the ADF-STEM image as the EELS spectrum image was attained using a TEAM 0.5 aberration corrected instrument operating at 80 kV at Lawrence Berkeley National Laboratory, equipped with a high-brightness Schottky-field emission electron source. The ADF-STEM image and EELS elemental maps were acquired using a Gatan Efinia spectrometer, with a collection angle of 52 mrad and a convergence angle of 30 mrad.

2.6. Energy-Dispersive X-ray Spectroscopy. Cycled electrodes were disassembled in an argon-filled glovebox and washed with acetonitrile before being scraped and dispersed onto TEM carbon grids. As-prepared TEM grids were analyzed using a FEI Tecnai Osiris system at 200 kV accelerating voltage. Four windowless silicon drift detectors placed at 90° with respect to each other were used to obtain the chemical maps. A 1 nA beam was used in a $\sim 512 \times 512$ array with a 25 μs dwell time for $\sim$10 min. The EDS data was then quantified and deconvoluted using the Cliff-Lorimer method.

3. RESULTS AND DISCUSSION

To understand the effect of the binder on the electrochemical performance and cycle life first, the coin cells were prepared in

the same way, albeit with different binders (PAA and CMC). This would help to rule out the effects that could be caused by the electrolyte or silicon shape and morphology. As shown in Figure 1a, the first cycle discharge capacity is 3303 mA h/g and charge capacity is 2540 mA h/g for the half-cell with the CMC binder and 3650 mA h/g for first cycle discharge and 3088 mA h/g charge capacity for the half-cell with the PAA binder. The first discharge capacity here refers to the lithiation of silicon, and first charge capacity refers to delithiation. The first cycle Coulombic efficiency is also 7.7% higher with PAA binder at 84.6 versus 76.9% for the CMC case. Apart from the first cycle metrics, the capacity retention is also an important parameter in evaluating cycle life. Although both the half-cells have a similar drop in capacity of $\sim$500 mA h/g in the first 30 cycles, after 100 cycles, the PAA binder allows the silicon anode to have a higher capacity retention of 80%, whereas the CMC binder leads to a faster decay in the cycling performance and a lower capacity retention of 73% (Figure 1b).

The SEM images shown in Figure 1c indicate the volume expansion that occurs in the silicon anodes. The large volume expansion leads to a much thicker electrode at the end of 100 cycles as seen for both the anodes with the CMC and PAA binders. Both silicon electrodes have similar thickness and cross-sectional morphology at the end of the 1st and 5th cycles. This is expected because the capacity fade (seen in Figure 1b) is similar in both cases until 30 cycles. However, after 100 cycles, the cross-sectional morphology of the cycled anodes is markedly different as seen in the right panel in Figure 1e,h. While the electrode with the CMC binder (Figure 1e) shows a large
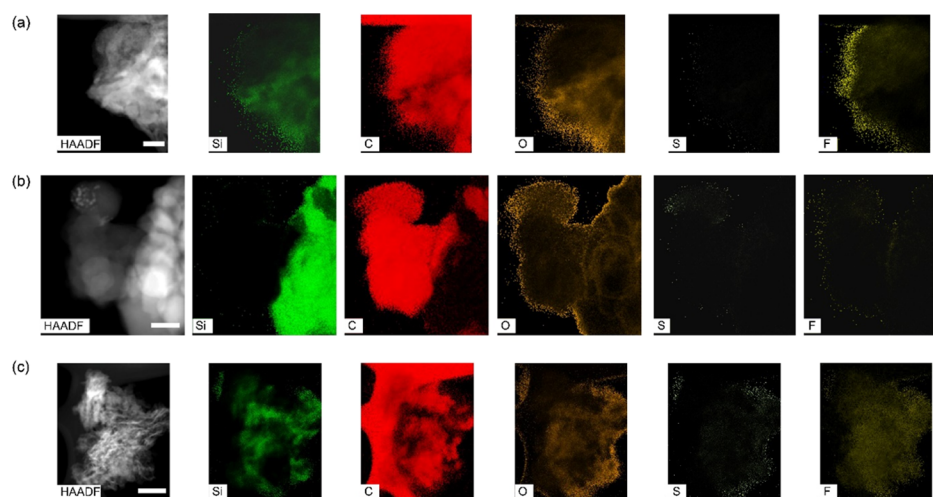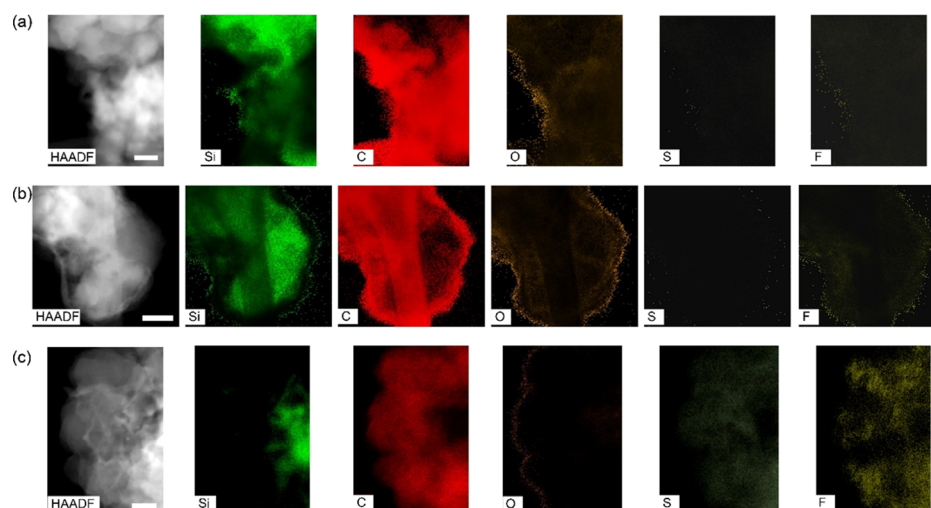
Figure 3. STEM-EDS mapping of silicon electrode with CMC binder after lithiation (a), after 5 cycles (b), and after 100 cycles (c). The maps show the elemental constitution of the SEI. Intermixing of F with silicon is seen after 100 cycles but the sulfur is still only present in the envelope region around the silicon carbon composite. The scale bars are 70 (a), 60 (b), and 200 nm (c). The sulfur and F maps have been edited to allow greater visibility because the original maps were not clearly visible due to the darker colors used for EDX mapping. The edited maps do not change any of the conclusions. The original maps and individual edits are provided in Supporting Information Figures S1−S8.

number of cracks and a nonuniform electrode surface, indicative of possible isolation of parts of the silicon anode, the SEM for the electrode with the PAA binder (Figure 1h) shows a much smoother and uniform cross section, with no cracks, indicating minimal to no isolation of the silicon anode.

The cross-sectional SEM and electrochemical performance indicate that the PAA binder functions better with the silicon anode, both in terms of capacity retention and in allowing the electrode morphology to be preserved. To better understand the reason for the observed differences, we turn toward STEM-EELS and EDX. Figure 2a shows the EELS spectra for anodes with the CMC and PAA binders. The spectra show that the bulk chemical composition of the electrodes is (a) similar for both cases and (b) preserved after 100 cycles for both PAA and CMC electrodes. The EELS spectra for the bulk of the electrode for CMC and PAA binders show a peak at 100 eV, which corresponds to Li_xSi.[33,34] The surface of the electrodes though shows the formation of a native oxide layer (Li_xSiO_y), indicated by the characteristic Si-L edge peaks for amorphous silicon oxide at 108, 115, 130.9, and 158.9 eV.[33,34] This surface oxide layer is present after the 1st cycle and persists even after 100 cycles, indicating a robust oxide surface on both electrodes. The formation of LiF is also confirmed as an SEI component in the 1st cycle. Figure 2c shows the Li K-edge after the 1st cycle for PAA and CMC electrodes with the LiF salt spectra included for comparison. The Li K-edge for LiF matches well with the peaks for CMC and PAA electrodes at 60.2 eV. The F K-edge at 695.4 eV, shown in Figure 2d, also matches well for both the samples. The formation of LiF occurs because of the decomposition of the LiFSI salt and has been proposed in literature to have a favorable effect on the cycle retention. In brief, a LiF inorganic layer, which is formed closer to the electrode surface in conjunction with the organic decomposition products, leads to a stable SEI which prevents further electrolyte decomposition.[30,35] Recently, artificial LiF coating has also been explored for silicon electrodes but with limited success that the authors attributed to the fact that LiF formed in situ with the organic SEI species provides greater mechanical strength, compared to the inorganic LiF films.[36] This mechanism of LiF formation has also been used to explain the role of the FEC additive in the

electrolyte.[30−32] Thus, understanding the rate of LiF formation and its nanoscale distribution as a function of the binder used is critical in explaining the stability of the SEI formed on the silicon anode and hence its cycling capacity retention.

Although EELS provides insights into the chemical composition of the SEI, in order to observe its nanoscale distribution on silicon particles, we used STEM-EDS. The Si map indicates the distribution of the nanoparticle-active material; the F and S signals are derived from the decomposition of the electrolyte salt (LiFSI) (Figure 3a−c). The LiFSI decomposes first to LiF due to the cleavage of the F−S bond (seen from the F 1s XPS spectra ~688 eV in Figure 5b). LiFSI further decomposes to sulfates (Li_2SO_4, SO_x^- species) and sulfides (Li_xS/Li_2S) (S 2p spectra in Figure 5d).[29,35,37−39] The oxygen is possibly from the native oxide layer formed and the sulfate SEI species. The difference between the O and S EDX spectra is used to later understand the formation and presence of sulfide versus sulfate species. As seen for the CMC binder-based electrode, after the 1st cycle, the F signals indicate a covering layer around the silicon−carbon composite with a low intensity of sulfur, which is also seen in the same region (Figure 3a). This is indicative of the LiF formed and sulfates/sulfides being present in the SEI (more evidence presented in Figure 5d through XPS spectra). The O maps also correlate well with the Si map. Separate regions for silicon and carbon are also seen. From Figure 3b, we see that this surface layer for F and S also exists after 5 cycles, indicating possibly no change in the chemical distribution of the LiF and sulfates/sulfides around the silicon carbon composite at the nanoscale. After 100 cycles though, the F and sulfur maps are markedly different (Figure 3c). Although the sulfates and sulfides are still concentrated in the covering layer, the LiF is now distributed more uniformly across the silicon particles, indicating a possible intermixing between the silicon and LiF. The reason for this mixing, if any, is still not fully understood. The F map spread across the entire silicon region can possibly point to the presence of a large amount of LiF in the SEI. However, closer to the silicon particles, there seems to be a much smaller amount of sulfates and sulfides present. Such a nanoscale study of the chemical distribution of silicon anode at

Figure 4. STEM-EDS mapping of silicon electrode with PAA binder after lithiation (a), after 5 cycles (b), and after 100 cycles (c). The maps show the elemental constitution of the SEI. Intermixing of F and S with silicon is seen after 100 cycles which is different compared to the CMC binder. The scale bars are 50 (a), 50 (b), and 40 nm (c). The sulfur and F maps have been edited to allow greater visibility because the original maps were not clearly visible due to the darker colors used for EDX mapping. The edited maps do not change any of the conclusions. The original maps and individual edits are provided in Supporting Information Figures S2−S8.
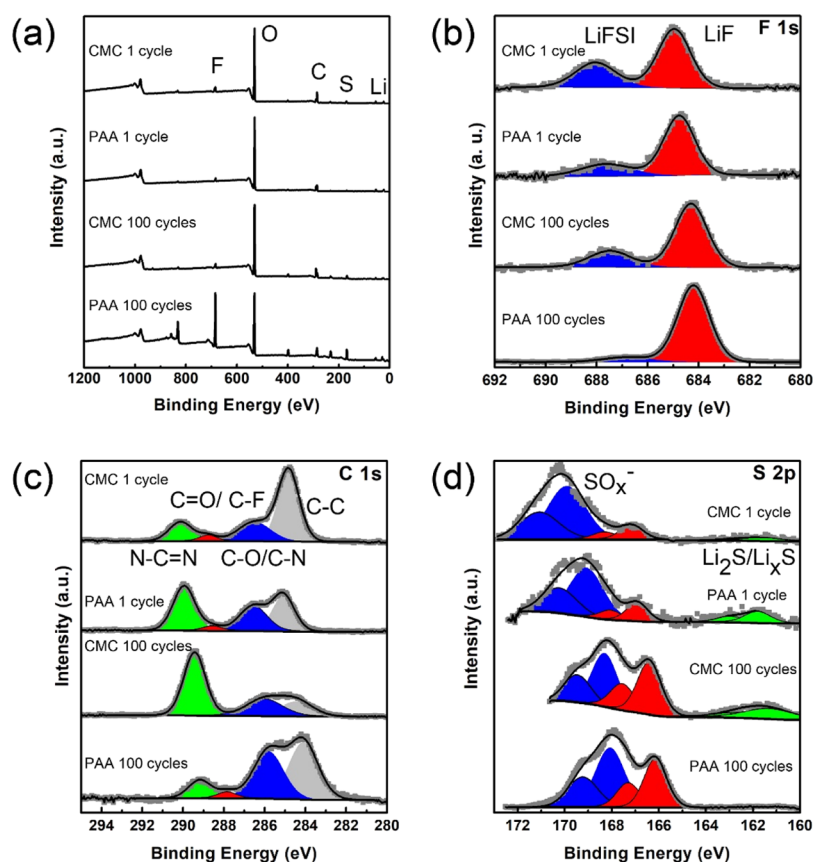
Figure 5. (a) Comparison of the XPS spectra of silicon electrodes with CMC and PAA binder. The chemical signature of the species formed is the same in each case after the 1st cycle and after 100 cycles. (b) F 1s spectra show the rapid consumption of LiFSI and formation of LiF in the presence of PAA binder right after the 1st cycle, whereas the electrode in the presence of CMC binder has a slower decomposition of LiFSI as obtained from the XPS fitting peak areas %. The PAA and CMC curves indicate that this trend continues until after 100 cycles. (c,d) Differences in the carbonate and SO_x^- species formed are observed for both CMC and PAA binder-based electrodes.

different cycle numbers is thus very valuable in identifying the evolution of the SEI.

Comparing the EDX maps for the CMC binder samples with the PAA binder, we see a similar covering layer around the

silicon carbon composite being formed for LiF and SO_x^-/S^{2-} species, both at the end of the 1st cycle and 5th cycle. This is seen in Figure 4 panels (a) and (b). This indicates that with both of the binders, the silicon anode SEI initially evolves in the same

fashion, spatially and chemically and both at the macroscale and nanoscale. The electrochemical performance, cycling retention, SEM morphology, and EDX and EELS results all point to this same conclusion (minor differences in the exact chemical species formed could be different as seen by XPS spectra but the nature of the evolution still progresses in the same way). However, after 100 cycles, the EDX maps show that although in the CMC case (Figure 3c), F is distributed more homogeneously with the silicon but S is not, the S and F distributions are more homogeneous with the PAA binder. This is indicative of the fact that the LiF forms all across the silicon surface and the SO_x^-/S^{2-} species are only seen in the covering layer with CMC but with PAA, both the LiF and S^{2-} species are formed all across the silicon surface (Figure 4c). Thus, there is a clear difference in the amount and distribution of sulfur formed in both cases. In the PAA case, the species after 100 cycles is identified as S^{2-} and not SO_x^- because the O maps at 100 cycles are only on the covering layer and not concurrent with the S maps, indicating the presence of sulfides closer to the silicon particles at a much higher intensity than in the initial cycles. (The EDX maps for S give very low intensity in the first cycles but XPS results in Figure 5 show the presence of both sulfates and sulfides after the 1st cycle.)

To get quantitative information regarding how the LiF and sulfates/sulfides species are formed across cycles through the bulk of the electrode surface, we use XPS. Figure 5a shows that although chemically the compositional makeup of the electrodes is the same with both binders, differences in the intensities are apparent after 100 cycles. [Details about accuracy of the XPS fits through comparison of the full width at half-maximum (fwhm) for each element and the peak area percentages are provided in Supporting Information Tables S1 and S2.] The deconvolution of F 1s spectra shows 2 peaks with binding energies of 684.6 and 687.9 eV. The peak at 684.6 eV is attributed to LiF[35,40] and at 687.9 eV to pristine LiFSI salt.[35] Comparing the fitting of the LiF peak for the F 1s spectra after 1 cycle for CMC and PAA, a peak area percentage of 65% ($\pm$0.85) and 74% ($\pm$2.12), respectively, is obtained for each case. A larger peak area of LiF (in comparison to LiFSI) indicates a faster consumption of LiFSI salt and a larger amount of LiF formation right after the 1st cycle for the PAA case (Figure 5b). The amount of LiF formed is also confirmed through depth profiling in the XPS (Supporting Information Figures S9 and S10), which shows a similar trend even after 10 min of etching. A comparison of the peak area percentages before and after etching is also shown in Supporting Information Table S3.

Figure 5c shows the deconvolution of the C 1s spectra. The peak at 285 eV can be attributed to C–C bonds. Peaks at 286 and 290 eV can be attributed to C–N and N–C≡N, respectively, that are a signature of the IL; the large peak for CMC samples at 100 cycles could possibly be due to incomplete washing. The peak at 286 eV could also be attributed to C–O, arising from the binder itself that consists of –COOH and C–OH groups. The peak at 288 eV is a signature of the C–F bond from the LiFSI salt, or possibly from C=O bonds again arising from the binder itself.[17] Using XPS itself, an accurate representation of the peak assignment for C 1s might not be possible because of the presence of multiple carbon species both in the binder and the electrolyte. From Figure 5d, the deconvolution of the S 2p spectra reveals evidence of the detachment and reaction of the SO_2 group from FSI^- breakdown for both the CMC and PAA cases. The peak at binding energies of 162.5 and 163 eV corresponds to Li_xS/Li_2S.

Binding energy peaks at 166.5 and 168 eV are attributed to SO_x^- species formed, whereas the fittings at 168.5 and 170 eV correspond to Li_2SO_4.[29,35,37−39] The peaks at ~168−170 eV that are present in the samples at 100 cycles are also attributed to SO_x^- species. The S spectra shows that while for PAA after 1 cycle, small organic species such as sulfides are present in the SEI; this is not the case for CMC. After 100 cycles, the reverse occurs though, with the CMC electrode surface accumulating sulfides and almost no sulfide intensity (too low for any reasonable fitting) for the PAA electrode surface.

The XPS, EELS, and EDX spectra and maps hence provide a bulk to nanoscale understanding of the evolution of the SEI when different binders are used. This shows that the binder not only helps with the mechanical stability but also affects the SEI species formation and distribution, ultimately affecting the electrochemical stability of the silicon anode as well. The discussion based on the results follows through in three steps as shown by the schematic in Figure 6: (1) after the 1st cycle, LiF is
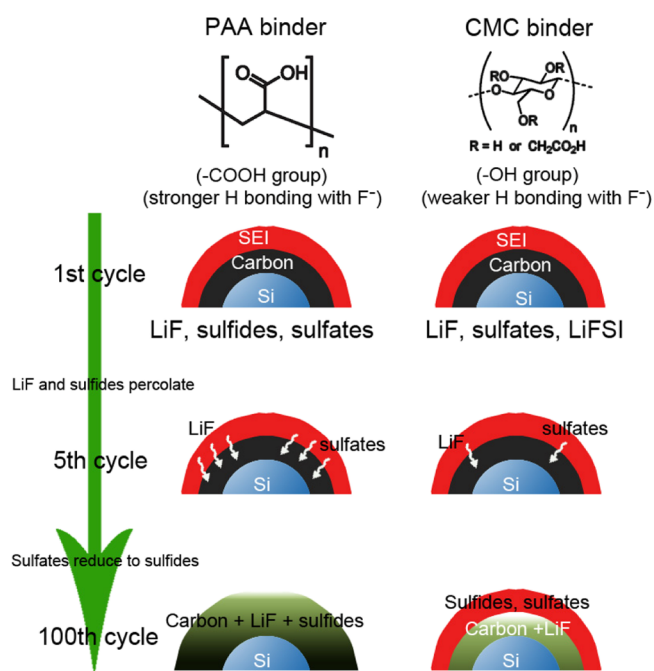
Figure 6. Schematic showing the proposed mechanism for the passivating effect of sulfides as part of the SEI in the presence of PAA binder. In the case of the PAA binder, the sulfides form a passivating layer closer to the silicon nanoparticles because of effective percolation of sulfates. With the CMC binders, the sulfides are present on the surface.

formed by the breakdown of FSI ion both in the presence of CMC and PAA binder. The signature of LiF formed is seen through EELS (Figure 2c,d) and F 1s XPS spectra (Figure 5b). The LiF meanwhile forms an enveloping layer around the silicon carbon composite for electrodes with CMC and PAA binder, respectively. This is evidenced by the EDX maps (Figures 3a and 4a). However, the breakdown of FSI^- is more rapid for the PAA case, as seen by XPS (Figure 5b). This could be attributed to the ability of PAA binder to form stronger hydrogen bonds with F^- (from LiFSI). We hypothesize that the higher density of carboxylic acid groups (–COOH) in PAA allows it to have a larger dipole moment that can cause the hydrogen bond (H⋯F) strength to be greater. This leads to the F^- group having a larger partial electronegative charge and being an effective leaving

group from the FSI anion when attacked by Li$^+$. Because of the −OH groups, CMC has lower hydrogen bond strength and F$^-$ is therefore a less effective leaving group, leading to slower LiF formation.

The ability of both CMC and PAA to form intermolecular hydrogen bonds (bonds between different chains), albeit with their own polymeric units, has been experimentally observed for PAA[41] and for CMC[42,43] using nuclear magnetic resonance and Fourier transform infrared (IR) spectroscopy. Clear broad peaks in the range of ∼2500−3500 cm^{-1} have been observed in the IR spectrum for each binder that can be attributed to the broadening of the −OH stretching peak because of hydrogen bonding.[44,45] Typical enthalpies of dimerization for small molecules, such as acetic acid, formic acid, and methanol, fall in the range of 15−17 kcal/mol for acids, with a value of 15.6 kcal/mol for acetic acid, whereas for methanol, this value is in the range of 1.7−5 kcal/mol based on the degree of dimerization.[46] This indicates that stronger intermolecular hydrogen bonding is seen in PAA (carboxylic acid group) as compared to that in CMC (hydroxyl group). The proposed mechanism and the ability of the binders to form hydrogen bonds of different strengths are also indirectly supported by a simple pH paper test. We apply the pH test to measure the concentration of H ions in the binder solution. A smaller pH indicates a greater concentration of H ions, which means that there are more polarizable H ions and thus the attached functional groups have a larger dipole moment. Figure S16 shows the pH test with the PAA binder solution having a pH ≈ 4 and CMC solution with a pH ≈ 7, which agrees well with our proposed mechanism.

Further, partial neutralization of PAA with LiOH to give LiPAA (which would lead to lower hydrogen-bonding strength) shows a lower peak area percentage for the LiF, indicating lower decomposition levels. The results are shown in Supporting Information Figures S11−S13. (A similar analysis with PVDF which is inactive with respect to hydrogen-bonding strength did not yield the same results possibly because of the presence of F in the binder that led to LiF formation; details are provided in Supporting Information Figures S14 and S15.)

(2) After 5 cycles, the spatial distribution of the chemical species as seen by EDX (Figures 3b and 4b) does not change, indicating that after the 1st cycle, the SEI composition further evolves in a similar way. The capacity retention (Figure 1b) and SEM morphology (Figure 1d,g) also agree with this mechanism. Ab initio molecular dynamics simulations have shown the formation of SO_2NSO_2F, $N(SO_2)_2$, and NSO_2 type species through multielectron reduction processes because of the decomposition of LiFSI salt with DME electrolyte.[28,47] However, since the exact mechanism of the decomposition of LiFSI salt has not been investigated, we believe that S═O species formed are continuously reduced to sulfides as the anode cycles.

(3) After 100 cycles, in the PAA case, a larger consumption of FSI anion is observed through the F 1s XPS spectra (Figure 5b, larger peak area % of LiF), whereas the pristine FSI anion signals are still seen with CMC binder (Figure 5b, smaller peak area % for LiF). Additional details are provided in Supporting Information Table S1. The EDX maps in both cases (Figures 3c and 4c) show the presence of F (indicative of LiF) closer to the silicon nanoparticles. Repeated volume expansion and contraction across cycles can allow percolation of the small LiF molecules, leaving the larger pristine FSI anions at the surface.

This can help explain the F distribution seen through the EDX map at the end of 100 cycles.

The observed difference in the sulfur and oxygen distribution at the end of 100 cycles between PAA and CMC binders is possibly due to the difference in the percolation rate of sulfates in the SEI based on the hydrogen-bonding strength and polarity of the binder. This mechanism is similar to the separation of molecules of varied size in column chromatography based on the charge and polarity of the matrix molecules through which the separating molecules percolate. The higher polarity of the −COOH group (from PAA) compared to −OH group (from CMC) leads to faster percolation of the reduced sulfate species toward the silicon nanoparticles.

In the presence of the PAA binder, its stronger intermolecular hydrogen-bonding strength with F$^-$ due to the −COOH functional group allows faster reduction of LiFSI to smaller molecules such as LiF and sulfates within the first few cycles. This allows the smaller sulfates to percolate easily across the carbon and binder (on repeated volume expansion). These sulfates then reduce to sulfides at lower voltages near the silicon surface. Thus, the sulfide signals from the S 2p XPS spectra for the PAA binder decrease after 100 cycles as it has been redistributed into the bulk. With the CMC binder, the weaker intermolecular hydrogen bond strength with F$^-$ coming from −OH functional group allows slower decomposition of LiFSI and no sulfide formation at the end of the 1st cycle (Figure 5d). The presence of much bulkier pristine LiFSI salt leads to slower reduction of sulfates to sulfides. Thus, the sulfates, sulfides, and pristine LiFSI salt are now restricted to the surface as evidenced by the buildup of sulfides from the S 2p XPS spectra in Figure 5d. The −OH functional group also leads to slower percolation of the sulfates because of weaker hydrogen bonding. The passivating nature of sulfides on the electrochemical perform- ance has been observed for solid-state batteries.[48] Such a passivating effect on individual silicon nanoparticles in the presence of PAA binder, in addition to the faster resulting LiF formation, could explain the greater capacity retention for these electrodes as compared to CMC-based electrodes.

4. CONCLUSIONS

In conclusion, the role of binder on the rate of SEI formation, the SEI composition, and its spatial distribution has been investigated. The silicon anode SEI directly affects the cell performance and surface morphology. Although the PAA and CMC binders start off similarly, the PAA binder shows greater capacity retention. EDX, EELS, and XPS were used to investigate the mechanism involved for this effect, and a simple model for the LiF formation rate was proposed based on the differences in the hydrogen-bonding strength in both the binders. The LiF formation rate directly affects the formation of small inorganic SEI species (LiF and sulfides) which percolate through the electrode based again on the bonding strength of the binder. EDX maps show that after the 1st and 5th cycles, the LiF and sulfide decomposition products in the SEI are enveloped around the electrode surfaces for both CMC and PAA binders. After 100 cycles, the LiF is present around individual silicon nanoparticles because of its formation in the first cycle itself, but a homogeneous sulfide distribution is only seen with the PAA binder because of its ability to allow greater percolation based on its bonding strength. This homogeneous sulfide distribution leads to a passivating effect on individual particles, resulting in improved capacity retention in silicon anodes. Such a nanoscale investigation of the role of the binder is crucial for the silicon

anode to understand its long-term cycle life capability. Our study provides an understanding as to why tailoring the binder is important for silicon anodes not only from a mechanical stability aspect but also from an electrochemical aspect.

■ ASSOCIATED CONTENT

Ⓢ Supporting Information

The Supporting Information is available free of charge on the ACS Publications website at DOI: 10.1021/acs.chemmater.8b05020.

> Raw data for the EDX maps, the comparison for the raw data versus modified images for F and S maps for each case, the FWHM parameters from the XPS fitting for each peak for each sample for both F 1s and S 2p, XPS depth etching to compare the LiF and LiFSI peak area ratio for LiPAA, PAA, and CMC samples, electrochemical performance and LiF peak area ratio for samples with LiPAA binder and PVDF binder, and the pH test for CMC and PAA electrodes are all shown in the Supporting Information. (PDF)

■ AUTHOR INFORMATION

Corresponding Author

*E-mail: shmeng@ucsd.edu.

ORCID ⦿

Pritesh Parikh: 0000-0003-2258-5719
Xuefeng Wang: 0000-0001-9666-8942
Ying Shirley Meng: 0000-0001-8936-8845

Author Contributions

The manuscript was written through contributions of all authors. All authors have given approval to the final version of the manuscript.

Notes

The authors declare no competing financial interest.

■ ACKNOWLEDGMENTS

■ REFERENCES

(1) Seroussi, H. Fate and future climatic role of polar ice sheets. *Nature* **2019**, *566*, 48−49.

(2) Lin, H.; et al. Ambient particulate matter air pollution associated with acute respiratory distress syndrome in Guangzhou, China. *J. Exposure Sci. Environ. Epidemiol.* **2018**, *28*, 392−399.

(3) Lashof, D. A.; Ahuja, D. R. Relative contributions of greenhouse gas emissions to global warming. *Nature* **1990**, *344*, 529−531.

(4) Meinshausen, M.; et al. Greenhouse-gas emission targets for limiting global warming to 2 °C. *Nature* **2009**, *458*, 1158−1162.

(5) Nitta, N.; Wu, F.; Lee, J. T.; Yushin, G. Li-ion battery materials: present and future. *Mater. Today* **2015**, *18*, 252−264.

(6) Kasavajjula, U.; Wang, C.; Appleby, A. J. Nano- and bulk-silicon-based insertion anodes for lithium-ion secondary cells. *J. Power Sources* **2007**, *163*, 1003−1039.

(7) Zhang, W.-J. A review of the electrochemical performance of alloy anodes for lithium-ion batteries. *J. Power Sources* **2011**, *196*, 13−24.

(8) Goriparti, S.; et al. Review on recent progress of nanostructured anode materials for Li-ion batteries. *J. Power Sources* **2014**, *257*, 421−443.

(9) Li, J.-Y.; et al. Research progress regarding Si-based anode materials towards practical application in high energy density Li-ion batteries. *Mater. Chem. Front.* **2017**, *1*, 1691−1708.

(10) Tamirat, A. G.; et al. Highly stable carbon coated Mg2Si intermetallic nanoparticles for lithium-ion battery anode. *J. Power Sources* **2018**, *384*, 10−17.

(11) Wang, W.; et al. Silicon and Carbon Nanocomposite Spheres with Enhanced Electrochemical Performance for Full Cell Lithium Ion Batteries. *Sci. Rep.* **2017**, *7*, 44838.

(12) Wu, Q.; et al. Investigations of Si Thin Films as Anode of Lithium-Ion Batteries. *ACS Appl. Mater. Interfaces* **2018**, *10*, 3487−3494.

(13) Mukanova, A.; Jetybayeva, A.; Myung, S.-T.; Kim, S.-S.; Bakenov, Z. A mini-review on the development of Si-based thin film anodes for Li-ion batteries. *Mater. Today Energy* **2018**, *9*, 49−66.

(14) Jia, H.; et al. A novel approach to synthesize micrometer-sized porous silicon as a high performance anode for lithium-ion batteries. *Nano Energy* **2018**, *50*, 589−597.

(15) Sohn, M.; et al. Microstructure Controlled Porous Silicon Particles as a High Capacity Lithium Storage Material via Dual Step Pore Engineering. *Adv. Funct. Mater.* **2018**, *28*, 1800855.

(16) Sakabe, J.; Ohta, N.; Ohnishi, T.; Mitsuishi, K.; Takada, K. Porous amorphous silicon film anodes for high-capacity and stable all-solid-state lithium batteries. *Commun. Chem.* **2018**, *1*, 24.

(17) Shobukawa, H.; Shin, J.; Alvarado, J.; Rustomji, C. S.; Meng, Y. S. Electrochemical reaction and surface chemistry for performance enhancement of a Si composite anode using a bis(fluorosulfonyl)-imide-based ionic liquid. *J. Mater. Chem. A* **2016**, *4*, 15117−15125.

(18) Liu, X. H.; et al. Size-Dependent Fracture of Silicon Nanoparticles During Lithiation. *ACS Nano* **2012**, *6*, 1522−1531.

(19) Choi, S.; Kwon, T.-w.; Coskun, A.; Choi, J. W. Highly elastic binders integrating polyrotaxanes for silicon microparticle anodes in lithium ion batteries. *Science* **2017**, *357*, 279−283.

(20) Liu, G.; et al. Polymers with Tailored Electronic Structure for High Capacity Lithium Battery Electrodes. *Adv. Mater.* **2011**, *23*, 4679−4683.

(21) Wang, C.; et al. Self-healing chemistry enables the stable operation of silicon microparticle anodes for high-energy lithium-ion batteries. *Nat. Chem.* **2013**, *5*, 1042−1048.

(22) Wu, M.; et al. Toward an Ideal Polymer Binder Design for High-Capacity Battery Anodes. *J. Am. Chem. Soc.* **2013**, *135*, 12048−12056.

(23) Hu, B.; et al. The existence of optimal molecular weight for poly(acrylic acid) binders in silicon/graphite composite anode for lithium-ion batteries. *J. Power Sources* **2018**, *378*, 671−676.

(24) Magasinski, A.; et al. Toward Efficient Binders for Li-Ion Battery Si-Based Anodes: Polyacrylic Acid. *ACS Appl. Mater. Interfaces* **2010**, *2*, 3004−3010.

(25) Erk, C.; Brezesinski, T.; Sommer, H.; Schneider, R.; Janek, J. Toward Silicon Anodes for Next-Generation Lithium Ion Batteries: A Comparative Performance Study of Various Polymer Binders and Silicon Nanopowders. *ACS Appl. Mater. Interfaces* **2013**, *5*, 7299−7307.

(26) Karkar, Z.; Guyomard, D.; Roué, L.; Lestriez, B. A comparative study of polyacrylic acid (PAA) and carboxymethyl cellulose (CMC) binders for Si-based electrodes. *Electrochim. Acta* **2017**, *258*, 453−466.

(27) Komaba, S.; et al. Comparative Study of Sodium Polyacrylate and Poly(vinylidene fluoride) as Binders for High Capacity Si–Graphite Composite Negative Electrodes in Li-Ion Batteries. *J. Phys. Chem. C* **2012**, *116*, 1380−1389.

(28) Kerner, M.; Plylahan, N.; Scheers, J.; Johansson, P. Ionic liquid based lithium battery electrolytes: fundamental benefits of utilising both TFSI and FSI anions? *Phys. Chem. Chem. Phys.* **2015**, *17*, 19569−19581.

(29) Piper, D. M.; et al. Stable silicon-ionic liquid interface for next-generation lithium-ion batteries. *Nat. Commun.* **2015**, *6*, 6230.

(30) Schroder, K.; et al. The Effect of Fluoroethylene Carbonate as an Additive on the Solid Electrolyte Interphase on Silicon Lithium-Ion Electrodes. *Chem. Mater.* **2015**, *27*, 5531−5542.

(31) Xu, C.; et al. Improved Performance of the Silicon Anode for Li-Ion Batteries: Understanding the Surface Modification Mechanism of Fluoroethylene Carbonate as an Effective Electrolyte Additive. *Chem. Mater.* **2015**, *27*, 2591−2599.

(32) Nakai, H.; Kubota, T.; Kita, A.; Kawashima, A. Investigation of the Solid Electrolyte Interphase Formed by Fluoroethylene Carbonate on Si Electrodes. *J. Electrochem. Soc.* **2011**, *158*, A798−A801.

(33) Ewels, P.; Sikora, T.; Serin, V.; Ewels, C. P.; Lajaunie, L. A Complete Overhaul of the Electron Energy-Loss Spectroscopy and X-Ray Absorption Spectroscopy Database: eelsdb.eu. *Microsc. Microanal.* **2016**, *22*, 717−724.

(34) Sina, M.; et al. Direct Visualization of the Solid Electrolyte Interphase and Its Effects on Silicon Electrochemical Performance. *Adv. Mater. Interfaces* **2016**, *3*, 1600438.

(35) Eshetu, G. G.; et al. In-Depth Interfacial Chemistry and Reactivity Focused Investigation of Lithium−Imide- and Lithium−Imidazole-Based Electrolytes. *ACS Appl. Mater. Interfaces* **2016**, *8*, 16087−16100.

(36) Haruta, M.; Kijima, Y.; Hioki, R.; Doi, T.; Inaba, M. Artificial lithium fluoride surface coating on silicon negative electrodes for the inhibition of electrolyte decomposition in lithium-ion batteries: visualization of solid electrolyte interphase by in-situ AFM. *Nanoscale* **2018**, *10*, 17257−17264.

(37) Philippe, B.; et al. Improved Performances of Nanosilicon Electrodes Using the Salt LiFSI: A Photoelectron Spectroscopy Study. *J. Am. Chem. Soc.* **2013**, *135*, 9829−9842.

(38) Kim, H.; et al. In Situ Formation of Protective Coatings on Sulfur Cathodes in Lithium Batteries with LiFSI-Based Organic Electrolytes. *Adv. Energy Mater.* **2015**, *5*, 1401792.

(39) Takada, K.; et al. Unusual Passivation Ability of Super-concentrated Electrolytes toward Hard Carbon Negative Electrodes in Sodium-Ion Batteries. *ACS Appl. Mater. Interfaces* **2017**, *9*, 33802−33809.

(40) Verma, P.; Maire, P.; Novák, P. A review of the features and analyses of the solid electrolyte interphase in Li-ion batteries. *Electrochim. Acta* **2010**, *55*, 6332−6341.

(41) Dong, J.; Ozaki, Y.; Nakashima, K. Infrared, Raman, and Near-Infrared Spectroscopic Evidence for the Coexistence of Various Hydrogen-Bond Forms in Poly(acrylic acid). *Macromolecules* **1997**, *30*, 1111−1117.

(42) Said, H. M.; Abd Alla, S. G.; El-Naggar, A. W. M. Synthesis and characterization of novel gels based on carboxymethyl cellulose/acrylic acid prepared by electron beam irradiation. *React. Funct. Polym.* **2004**, *61*, 397−404.

(43) Li, W.; Sun, B.; Wu, P. Study on hydrogen bonds of carboxymethyl cellulose sodium film with two-dimensional correlation infrared spectroscopy. *Carbohydr. Polym.* **2009**, *78*, 454−461.

(44) Fessenden, R. J.; Fessenden, J. S. *Organic Chemistry*, 4th ed.; Brooks/Cole: California, 1990; Chapter 7, p 258, Chapter 9, p 332, Chapter 14, p 594.

(45) Streitwieser, A.; Heathcock, C. H.; Kosower, E. M. *Introduction to Organic Chemistry*, 4th ed.; Macmillan Publishing Company: New York, 1992; Chapter 17, p 467, Chapter 18, p 493.

(46) Jones, M. M.; Gilkerson, W. R.; Gallup, G. A. Hydrogen Bond Energies in Carboxylic Acids. *J. Chem. Phys.* **1952**, *20*, 1048.

(47) Camacho-Forero, L. E.; Balbuena, P. B. Elucidating electrolyte decomposition under electron-rich environments at the lithium-metal anode. *Phys. Chem. Chem. Phys.* **2017**, *19*, 30861−30873.

(48) Zhu, Y.; He, X.; Mo, Y. First principles study on electrochemical and chemical stability of solid electrolyte−electrode interfaces in all-solid-state Li-ion batteries. *J. Mater. Chem. A* **2016**, *4*, 3253−3266.